Research Article | Vol. 9, No. 10 | 1 Oct 2018 | BIOMEDICAL OPTICS EXPRESS 4702
Biomedical Optics EXPRESS

Dynamic blood flow phantom with negative and positive photoacoustic contrasts

HIND J. JAWAD,[1,2] MUSTAFA SARIMOLLAOGLU,[2] ALEXANDRU S. BIRIS,[3] AND VLADIMIR P. ZHAROV[2,*]

[1]*Department of Physics and Astronomy, University of Arkansas at Little Rock, 2801 S. University Ave., Little Rock, AR 72204, USA*
[2]*Arkansas Nanomedicine Center, University of Arkansas for Medical Sciences, 4301 W. Markham St., Little Rock, AR 72205, USA*
[3]*Center for Integrative Nanotechnology Sciences, University of Arkansas at Little Rock, 2801 S. University Ave., Little Rock, AR 72204, USA*
zharovvladimirp@uams.edu

Abstract: *In vivo* photoacoustic (PA) flow cytometry (PAFC) has great clinical potential for early, noninvasive diagnosis of cancer, infections (e.g., malaria and bacteremia), sickle anemia, and cardiovascular disorders, including stroke prevention through detection of circulating white clots with negative PA contrast. For clinical applications, this diagnostic platform still requires optimization and calibration. We have already demonstrated that this need can be partially addressed by *in vivo* examination of large mouse blood vessels, which are similar to human vessels used. Here, we present an alternative method for PAFC optimization that utilizes novel, clinically relevant phantoms resembling pigmented skin, tissue, vessels, and flowing blood. This phantom consists of a scattering-absorbing medium with a melanin layer and plastic tube with flowing beads to model light-absorbing red blood cells (RBCs) and circulating tumor cells (CTCs), as well as transparent beads to model white blood cells and clots. Using a laser diode, we demonstrated the extraordinary ability of PAFC to dynamically detect fast-moving mimic CTCs with positive PA contrast and white clots with negative PA contrast in an RBC background. Time-resolved detection of the delayed PA signals from blood vessels demonstrated complete suppression of the PA background from the modeled pigmented skin. This novel, medically relevant, dynamic blood flow phantom can be used to calibrate and maintain PAFC parameters for routine clinical applications.

1. Introduction

Photoacoustic (PA) flow cytometry (PAFC) has shown major clinical promise for detecting rare circulating tumor cells (CTCs), bacteria, clots, and other abnormal cells *in vivo* [1–3]. To do so, PAFC irradiates circulating targets with short laser pulses, then, using an ultrasound transducer attached to the skin, performs time-resolved detection of the acoustic waves (PA signals) caused by the laser [2]. Fast-growing applications of PAFC include diagnosis of malaria, sickle cell disease, and thromboembolic complications as well as detection of exosomes and nanoparticles [2–10], PAFC is becoming a relatively universal diagnostic tool. In order to move towards human use, this platform requires optimizations and calibrations. Recently, we demonstrated that this need can be addressed through *in vivo* testing of relatively large mouse blood vessels (0.5–1 mm in diameter, such as jugular vein or aorta), which are similar in size, depth, and flow velocity to the blood vessels in the human hand [2]. However, this method is time-consuming and requires animal testing; a biomedically adequate, animal-free blood flow phantom that is fast, cost-effective, and well-suited for PAFC is still needed. Some tissue phantoms have already been developed for different purposes: 1) to verify the performance of a new system prior to clinical applications; 2) to optimize a system's parameters, including maximization of signal-to-noise ratio; and 3) to calibrate a device in order to improve the accuracy and reproducibility of its measurements [11-12]. Generally, the absorption and scattering properties of the tissue phantom are the

#330965 https://doi.org/10.1364/BOE.9.004702
Journal © 2018 Received 4 May 2018; revised 6 Jul 2018; accepted 18 Jul 2018; published 10 Sep 2018

Biomedical Optics EXPRESS

essential design considerations. In addition, for PA techniques, phantoms should have well-characterized, versatile, and stable thermal and acoustic parameters similar to those of biotissue [13–16].

Others have reported a variety of materials that have the appropriate properties for use in PA phantoms, such as agar, bovine gelatin, polyvinyl chloride plastisol (PVCP), polyvinyl alcohol, and silicon [17–21]. Recently, PVCP has been commonly used for PA system characterization and quality control because it has the necessary optical transparency, long-term stability (can be stored for up to 6 months), and tissue-like acoustic properties. Specifically, it has density and acoustic parameters similar to water and average sound speed of around 1,400 ms^{-1} [22-23]. However, because of its fast reaction with plastic materials, it should not contact with these materials [24]. Although polyester and epoxy also have the appropriate optical transparency and long-term stability, these materials have a number of limitations, such as high shear sound wave speeds and attenuation coefficients. Certain optical scatters and absorbers could be added to PVCP to make its properties similar to human tissue. For example, titanium dioxide (TiO_2) and zinc oxide (ZnO) might be used as scatter materials [13]. To provide absorption properties, the phantom can be altered by adding India ink, fluorescent dyes, and copper/nickel chloride [25].

However, little progress has been made in developing a blood vessel phantom with flowing liquid that has properties similar to real blood [3,26]. So far, most phantoms used with PA and ultrasonic techniques are static only or have slow-moving (< 1 mm/s) objects [27]. Thus, they cannot be used to verify the dynamic PAFC platform, in which the lifetime of circulating cells in the detection volume is in the range of 0.5-2 ms at the typical cell velocity of 3-7 cm/s in human vessels. PAFC platforms require a dynamic blood phantom to test their ability to detect and count flowing particles and cells. The current work fills this gap by demonstrating a novel blood flow phantom for testing of PAFC in dynamic mode.

2. Materials and methods

2.1 The principle of PAFC phantom

Development of dynamic phantoms is complicated by the fact that, in real biotissue (Fig. 1(a)), laser irradiation of blood vessels generates continual PA background signals associated with strong absorption of hemoglobin (Hb) in many red blood cells (RBCs) in the detection volume. To be detectable in conventional positive contrast mode, targets must have higher localized absorption than the RBC background. In particular, when strongly absorbing CTCs (e.g., melanoma with intrinsic melanin or labeled with absorbing nanoparticles) or an RBC aggregate passes through the irradiated blood, a transient increase in localized absorption occurs, causing a sharp positive PA peak (Fig. 1(b), left). However, when weakly absorbing, platelet-rich white clots pass through the detection volume (Fig. 1(b), middle), a transient decrease in localized absorption occurs, causing a sharp negative PA peak [8]. A CTC-clot embolus with high and low absorbing localized zones will produce a pattern of positive and negative PA signals (Fig. 1(b), right) [2].

To address the need for a dynamic blood flow phantom strategically designed to meet the unique parameters of PAFC, we have developed a novel blood vessel and flow phantom to test PAFC in dynamic conditions. In our new phantom (Fig. 1(c)), RBCs with typical size found in humans (5–6 μm) are modeled by 5-μm magnetic beads with absorption in the near-infrared (NIR) range, close to that of RBCs (Fig. 1(d)). The concentration of magnetic beads was selected to match typical hematocrit levels, 0.3–0.4. Melanoma CTC clusters [3] or RBC aggregates are represented by larger magnetic beads, and white clots by transparent silica beads. PVCP was chosen to model biotissue, with TiO_2 nanoparticles providing the necessary scattering. Finally, a 200-μm-thick melanin layer was added on the surface of the phantom to represent pigmented skin.

Biomedical Optics EXPRESS

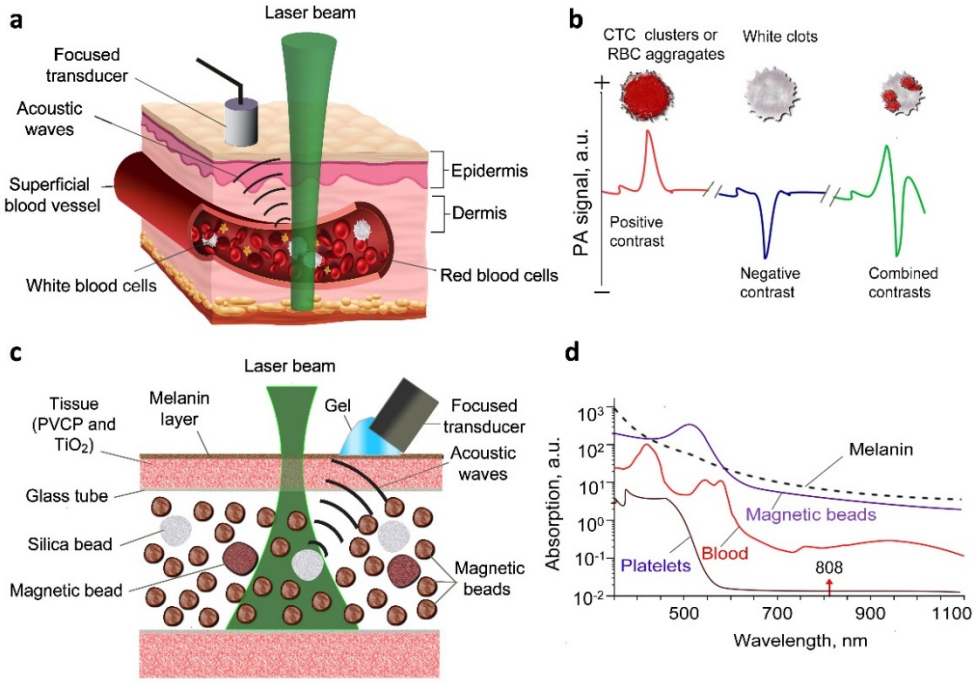

Fig. 1. (a) Schematic of real biotissue structure. (b) The typical PA trace with positive, negative, and mixed PA peak contrast [2]. (c) Schematics of blood vessel phantom. (d) Optical absorption of human blood, magnetic beads, platelets, and melanin [4-5].

2.2 Blood vessel phantom

To construct the blood vessel phantom, 30 ml of PVCP (2228 LP, M-F Manufacturing Co., TX) was heated to 200°C and mixed with 30 mg of TiO_2 powder (232033, Sigma-Aldrich Inc., Germany) via vigorous stirring to provide the necessary light attenuation and scattering. The solution was continuously mixed to minimize vapor loss and slowly cooled to 100°C over the course of 10 minutes, then poured into the mold. Before it cooled, it was shaken to prevent bubble formation. For the melanin layer, we used 30 mg of melanin powder (M2649, Sigma-Aldrich Inc.) and 20 ml of PVCP to provide optical properties similar to human tissue in the NIR range. Specifically, optical properties of human tissue at 808 nm (i.e., the laser wavelength used) are estimated to be as follows: reduced scattering coefficient μ_s = 6.80–9.84 cm^{-1} and absorption coefficient μ_a = 0.16–0.25 cm^{-1} [25]. A 200-μm-thick melanin layer was laid on top of the phantom surface which is similar to melanin layer thickness (100 μm to 300 μm) in humans [28]. The constituent materials for each desired layer were weighed by analytical balance and stirred. The powder items were fully mixed by hand as they were added to the PVCP in order to ensure good homogeneity. Following the addition of TiO_2 powder, the mixture was hand-mixed for 5 min. Before the solution was heated, hand mixing was utilized to prevent introduction of air bubbles into the mixture, which would impede homogeneity and quality. The phantom was cylindrical, with a diameter of 44 mm, and thickness of 10 mm. A thin glass tube (outer diameter: 1.5 mm, inner diameter: 1.1 mm, length: 75 mm) was put in the phantom at a depth of 1 mm, and both ends were connected to plastic tubes and a pump to provide blood circulation. The RBCs were represented by 5-μm magnetic particles (FCFM-4056-2, Spherotech Inc., IL), and CTCs by 8, 23, and 41-μm magnetic particles (Ferromagnetic particles, Spherotech Inc.), and white clots by 100-μm silica particles (110791101, BioSpec Products, Inc., OK).

Biomedical Optics EXPRESS

2.3 PAFC setup

The PAFC setup (Fig. 2(a)) was equipped with a laser diode (MM25004, Quantel Laser, France) with the following parameters: wavelength: 808 nm (Fig. 2(e)); pulse width: 25 ns; pulse repetition rate: 1–3 kHz; and pulse energy: up to 130 μJ. The laser diode bar had 20 emitters with a total length of 5 mm; each emitter was 8 × 200 μm (Fig. 2(c)).

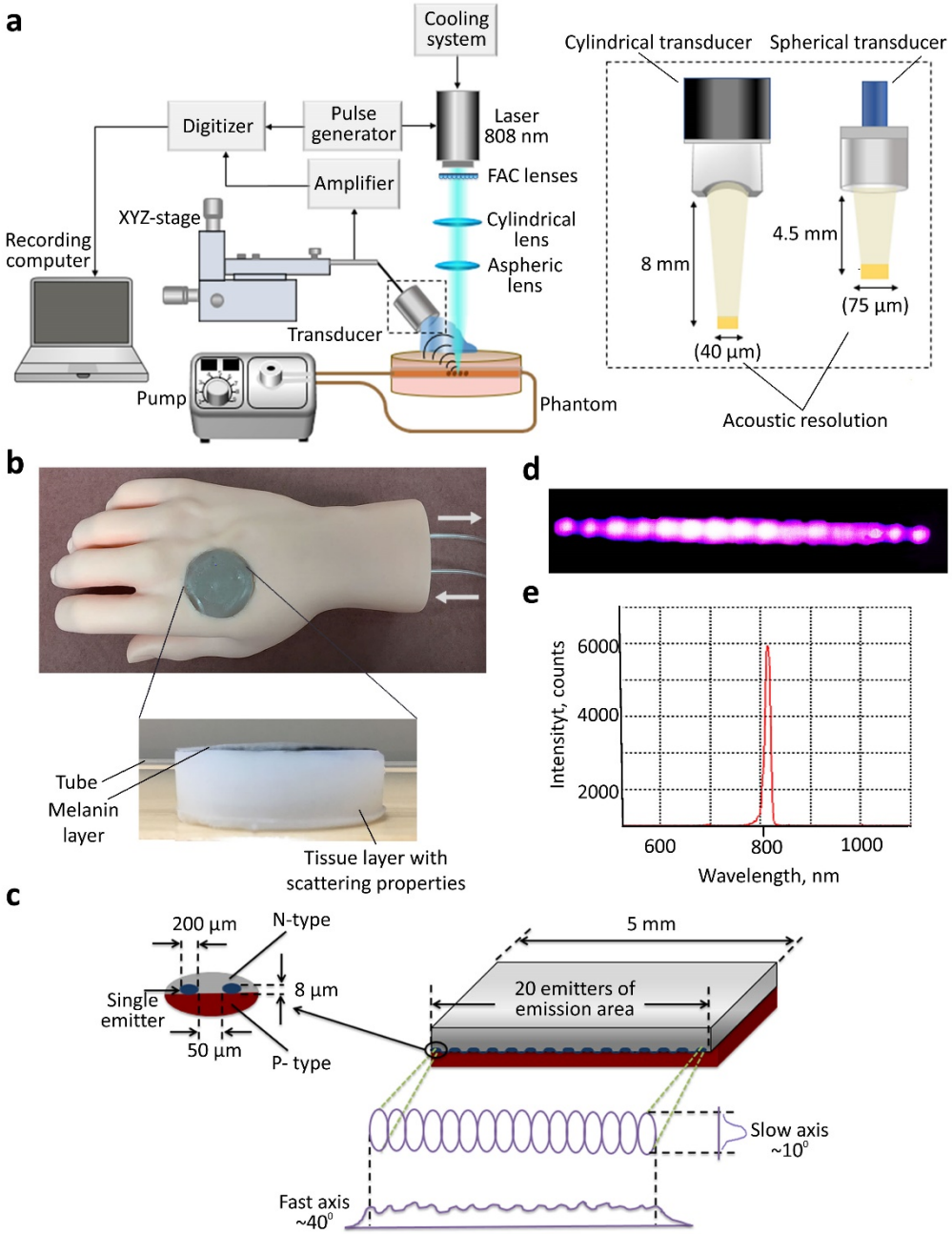

Fig. 2. (a) Schematic of PAFC system. (b) Image of the blood vessel phantom built in a hand phantom with connecting tubes inside "hand." (c) Schematic of the laser diode with a single bar. (d) Laser beam fragment image on the sample. (e) The typical spectral line of laser diode pulse with width of 25 ns at wavelength of 808 nm.

Biomedical Optics EXPRESS

The laser beam divergence was: 40° for the "fast axis" with a collimator (FAC) and 10° for the "slow axis." The FAC lenses had a focal point of 260 μm and diameter of 400 μm; these lenses were used to collimate the laser radiation in the fast axis direction with an angle of 2°. Laser radiation was delivered by a cylindrical lens (LJ1765L1-B; focal length: 38 mm, Thorlabs Inc., NJ) to collimate and reduce the beam size in the slow axis direction. A spherical lens (LA1252; focal length: 25 mm, Thorlabs Inc.) was used to focus and create the desired linear beam shape with a size of 1.7 mm × 80 μm (Fig. 2(d)) on the sample (Fig. 2(b)). The laser energy was controlled by an energy meter (PM100USB, S314C sensor, Thorlabs Inc.). The attenuation of laser energy in the optical scheme was 31%. The pulse energy after the optical scheme was adjusted to 38 μJ, which is sufficient for many applications. The PA signals were detected by the unfocused and focused ultrasound transducers. We used two types of ultrasound transducers: spherical (piezoelectric [PZT]; central frequency: 51.1 MHz; broadband resonance: 0.3–50 MHz, focal distance: 4.5 mm) and cylindrical (polyvinylidene fluoride [PVDF]; frequency band: 0.2–32 MHz; focal length: 8 mm) to compare their resolution (e.g., lateral acoustic resolution for spherical and cylindrical transducers was 75 μm and 40 μm, respectively). The transducer in the individual holder was mechanically fixed on the independent XYZ-stage at a ~35° angle to the optical axis that provides micrometer-precision adjustment of its position. The independent Z-stage was used to independently adjust the optical lens's focal point by moving the lens in the Z direction, with accuracy of 1 μm. Standard ultrasound gel was used for acoustic coupling between the transducer and phantom surface. These schematics allowed us to determine the optimal positions for the acoustic and optical focuses by maximizing the PA signal amplitudes. For example, first, the position of the optical lens was properly adjusted in the Z direction, then the 3-D position of the transducer, and then the lens again if necessary. As a result, the positions of the acoustic and optical focal points that provided maximal PA signals with good spatial resolution were achieved. A pulse generator was used to provide a signal to the driver of the laser diode, and a synchronized signal was sent to the data acquisition board (ATS9350, Alazar Technologies, Inc., Canada). PA signals were amplified by a preamplifier (AH-2010-100, Precision Acoustics Ltd, United Kingdom).

2.4 Human data

The PAFC results from the vessel phantom were compared with PA data from real blood vessels in healthy human volunteers, obtained in accordance with protocols approved by the University of Arkansas for Medical Sciences Institutional Review Board. The PA signals were acquired from the dorsum of the left hand.

2.5 Data processing

All measurements were performed at least three times, then the data sets were averaged. Counted data (M counts) are shown as $M \pm$ standard deviation.

3. Results

We selected the PAFC flow velocity initially in the range of 0.3-1 cm/s, with the possibility to reach up to 5-7 cm/s, which matches the blood velocity in most PAFC applications [2]. To prevent possible PA signal distortion from the non-uniform surface of the ultrasonic gel between the transducers and the samples, we used a small piece of glass between the optical lens and the biological sample. As we previously discovered [2, 3], spherical transducers provide higher signal-to-noise ratio (SNR) than cylindrical transducers at similar parameters because it has a smaller detection volume, and thus fewer RBCs are involved to produce background signals. However, the objects (e.g., CTCs) outside this volume would flow undetected. The focused cylindrical ultrasound transducer is better suited for PA measurement, because it provides a minimal detected volume due to high lateral resolution with simultaneous assessment of the entire cross-section of a vessel [3]. To verify the new

Biomedical Optics EXPRESS

phantom's performance, we compared the PA waveforms from human tissue and the phantom using focused spherical and cylindrical transducers. Both transducers demonstrated that the parameters of PA signals from the phantom and real vessels as well as those from the melanin layer and real skin are quite similar, although the sensitivity of the cylindrical transducer is a little lower than that of the spherical transducer (Fig. 3).

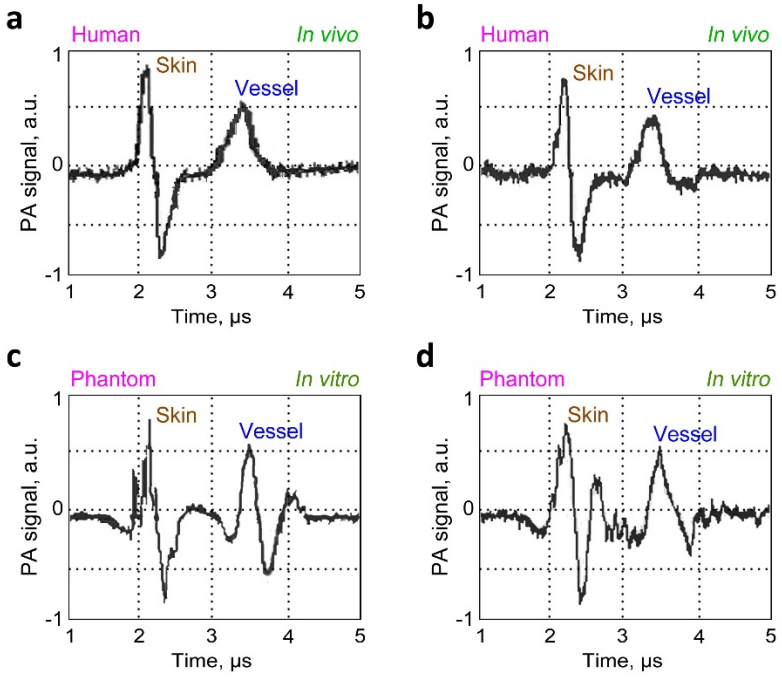

Fig. 3. (a and b) Typical examples of PA waveforms from ~1-mm vein at a depth of 1 mm in a human obtained with spherical (a) and cylindrical (b) transducers. (c and d) Typical examples of PA waveforms from the vessel phantom with similar properties to the human tissues acquired by spherical (c) and cylindrical (d) transducers.

We also compared the sensitivity of the two transducers by measuring the SNRs at different averaging times to demonstrate the optimal averaging time (Fig. 4).

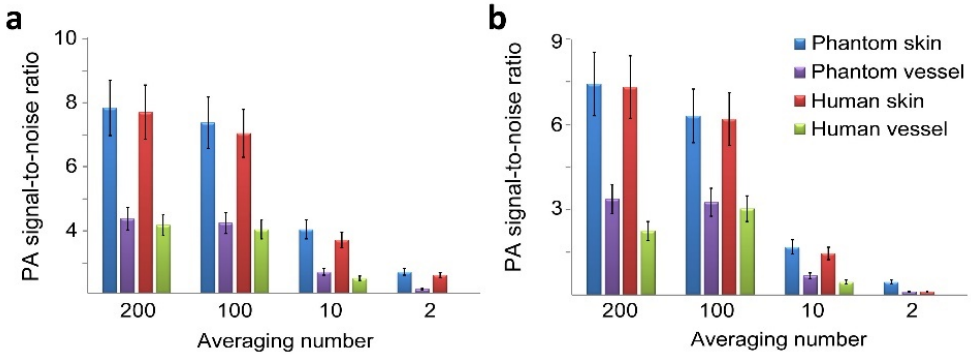

Fig. 4. Comparison of SNRs from a human and our phantom at different averaging numbers for spherical (a) and cylindrical (b) transducers.

To create the dynamic blood flow phantom, we mixed 250 μl of 5-μm absorbing magnetic beads as the RBC phantom with 1.5 ml of phosphate buffered saline (PBS) solution. These magnetic beads' absorption spectra in the NIR range was similar to the actual RBC spectra

Biomedical Optics EXPRESS

(gradually decreasing absorption from visible to the NIR range, Fig. 1(d)). These beads created constant PA background, as blood does in a real vessel (Fig. 5(a)). Then, we added 100 µl of 41-µm magnetic beads to model CTC clusters or RBC aggregates [2]. At a flow velocity of 5 mm/s, we observed transient narrow positive peaks above the blood background from the individual flowing beads (Fig. 5(c) and (e)). Increasing the signal averaging number led to a notable increase in SNRs. As predicated, the spherical transducers (Fig. 5(a), (c), and (e)) provided larger SNRs but lower peak numbers than cylindrical transducers (Fig. 5(b), (d), and (f)). In time-resolved detection, the PA signals from flowing large beads in the 1-mm-deep vessel phantom were distinguishable from the strong background PA signals from the melanin layer coming to the transducer with notable time delays (Fig. 3). Fig. 5 shows that the larger magnetic beads could be detected and identified by the PAFC system, even against a background of blood and skin. In order to estimate the ability of the dynamic blood phantom to detect white blood clots with lower absorption than RBCs, we diluted 30 mg of 100-µm silica beads with 1.5 ml of PBS suspension. We observed negative narrow PA contrast peaks associated with the quickly dropping absorption in more stronger absorption background of many 5 µm magnetic beads during passing of transparent beads the detection volume (Fig. 6). Consistent with data in Fig. 5, the spherical transducers produced a lower number of negative peaks than the cylindrical transducers. Using absorbing magnetic beads of various sizes (8, 23, and 41 µm) in the dynamic phantom at the same flow conditions, we observed positive PA peaks with different amplitudes associated with the different beads sizes. We have determined that PA signal amplitudes almost linearly depend on bead size (Fig. 7). Next, we mixed 41-µm absorbing magnetic beads and 100-µm transparent silica beads and monitored them in the same circulating system using PAFC. We observed positive and negative peaks, suggesting the potential of PAFC to simultaneously distinguish CTC or RBC aggregates with positive contrast and white clots with negative contrast as well as their clusters, called emboli (Fig. 8). The reproducibility of the PA signal amplitudes was evaluated by repeated PA signal measurement of the blood vessel phantom. This measurement was made hourly over a single day, then measured frequently within two weeks of the primary measurement (Fig. 9).

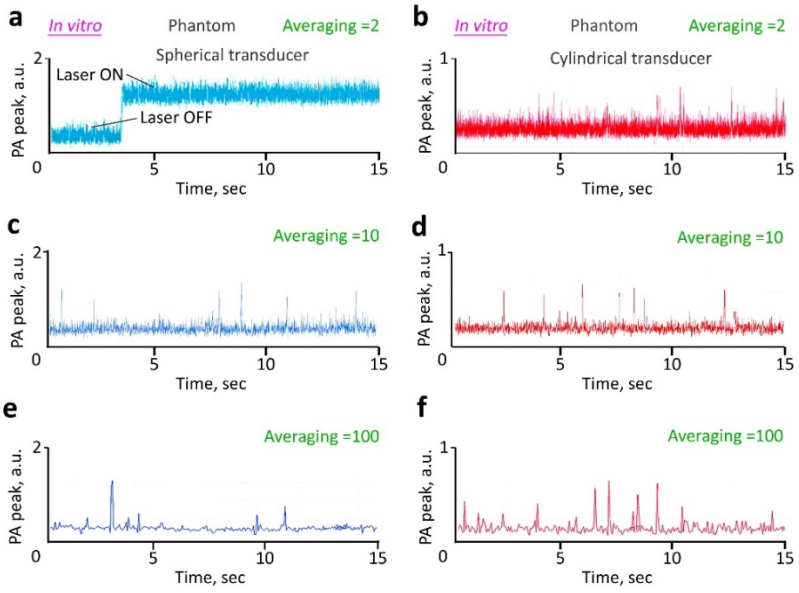

Fig. 5. (a) PA trace at laser off and on (as example). Typical PA traces from artificial blood consisted of 5-µm absorbing magnetic beads as RBC phantoms and rare 41-µm absorbing magnetic beads representing RBC aggregates or CTC clusters at different averaging signal times using spherical (a, c, e), and cylindrical (b, d, f) transducers.

Biomedical Optics EXPRESS

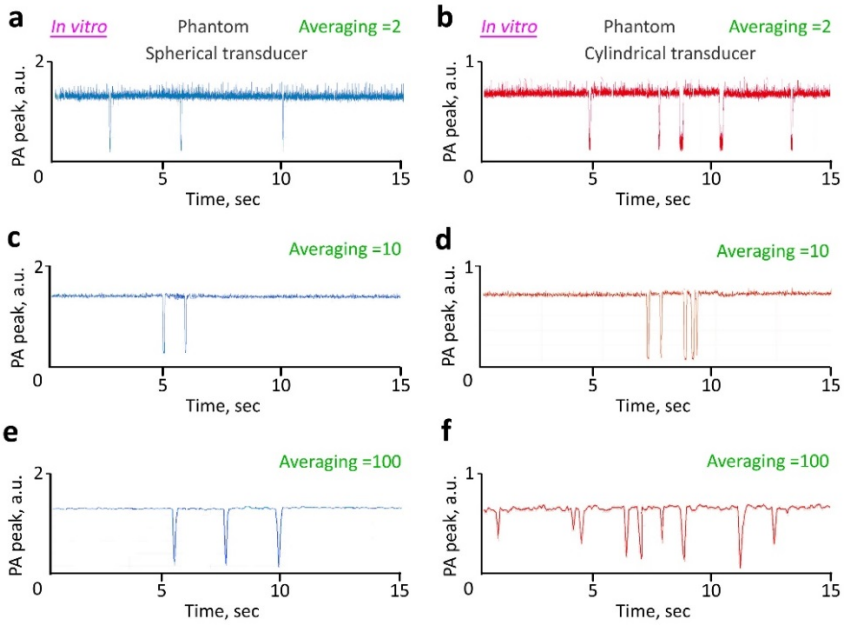

Fig. 6. Typical PA traces from artificial blood and 100-µm transparent silica particles as white clot phantom at different averaging signal numbers using spherical (a, c, e) and cylindrical (b, d, f) transducers.

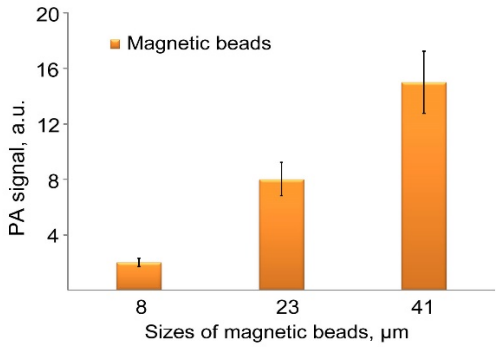

Fig. 7. PA signals with positive contrasts from absorbing magnetic beads with different sizes (8, 23, and 41 µm).

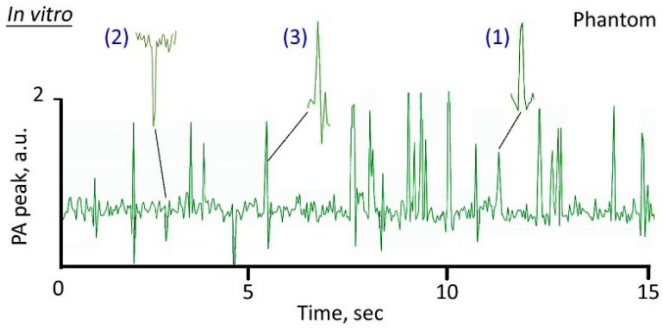

Fig. 8. Typical PA traces recorded during *in vitro* PAFC monitoring of individual magnetic (1), silica beads (2) and their clusters (3) in phantom model acquired by a spherical transducer.

Biomedical Optics EXPRESS

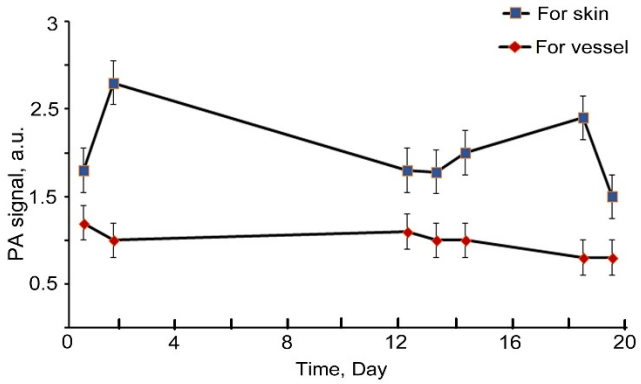

Fig. 9. The reproducibility of the PA signal amplitudes from skin and vessel phantom over time.

4. Discussion

In this work, a new dynamic blood vessel phantom for quick calibration and optimization of PAFC as a diagnostic platform with different acoustic schematics was demonstrated for the first time. While several phantoms have already been developed for PA imaging (e.g., refs. 11–16), they are only applicable for static or slow-moving (< 1 mm/s) objects [27]. Thus, they cannot be used for the calibration of the novel PAFC platform. This platform is both valuable and unique because it can detect abnormal circulating objects (e.g., tumor cells, bacterium, parasites, and sickle cells) moving in human vessels with a diameter of 1-3 mm and depth of 1-3 mm with a typical velocity of 3-7 cm/s [2–8]. Detection of such fast-moving objects has never been demonstrated with conventional PA techniques; particularly, PA microscopy and tomography have low time response [11,12]. Moreover, we introduced innovative negative-contrast PAFC for early detection of circulating clots, potentially enabling the prevention of strokes and, in some cases, heart attacks [2,8]. The existing PA phantoms cannot reproduce medically adequate conditions for these PAFC-based applications and, thus, cannot be used to verify and optimize the key PAFC parameters, including laser pulse rate (e.g., at low pulse rates, PAFC can miss many cells in the time gap between sequential laser pulses), high speed signal processing algorithms, signal averaging number (sensitivity of PAFC decreases at high averaging), and the transducer and amplifier bandwidth. All these parameters can now be tested with the phantom we presented.

The novel phantom provided PA signal patterns comparable to those from real blood vessels (Fig. 3, 4). Using this phantom, we demonstrated complete background suppression from strongly pigmented skin through time-resolved detection of PA signals from phantom blood vessels coming to the transducer with a significant time delay (Fig. 3). The phantom allows quick comparison of different ultrasound transducers and selection of the optimal signal averaging time for temporal resolution of fast-moving objects. The optical properties of the phantom measured via UV-Vis spectrophotometer (μ_a = 0.165 cm^{-1} and μ_s = 10 cm^{-1}) were close to those of real human tissue (μ_a in the range of 0.16–0.23 cm^{-1} and μ_s in the range of 6.80–9.84 cm^{-1}) [25].

As shown in Fig. 4, the performances of the spherical and cylindrical transducers are different. The PA signal amplitude from the spherical transducer was a little higher than that of the cylindrical transducer, although the latter provides more PA signals as it covers a larger detection volume. The phantom also allows the optimization of SNRs.

The laser diode demonstrated excellent performance in combination with PAFC and the new phantom. The amplitude of the PA background depended mainly on the pulse energy of the laser diode and the concentration of 5-µm magnetic beads as RBC phantom in the detection volume. The 41-µm magnetic beads representing CTC or RBC clusters with high

Biomedical Optics EXPRESS

local absorption were detectable as they passed through the irradiated area due to an increase in local absorption, which produced sharp peaks with positive PA contrast (see Fig. 5) In contrary, 100-μm transparent silica beads representing white clots generated a transient decrease in local absorption as they passed through the detection volume, which resulted in negative contrast peaks (Fig. 6). When comparing the transducers for positive and negative contrasts detection, we noticed that larger magnetic beads at a flow velocity of 5 mm/s (with averaging number 2) were detectable by the spherical and cylindrical transducers. With numbers averaging between 10 and 100, we were able to detect single beads using both transducers. According to our results presented in Fig. 6, the cylindrical transducer has a greater likelihood of detecting vast numbers of particles with low amplitude of negative PA peaks than the spherical transducer.

Figure 7 indicates that positive PA contrasts are a function of particle size due to the amount of laser beam absorption by the particles. Figure 8 shows a combined contrast from one particle cluster that contained both magnetic and silica beads. We observed a positive contrast from the magnetic bead and a negative contrast from the silica bead. Our analysis demonstrated that PAFC has good sensitivity for detecting combined particles. Figure 9 shows the PA signal amplitudes for pigmented skin and vessel over the first two weeks of testing. It indicates a minor difference in vessel skin's signal variation, and the standard deviation for the signals from the phantom skin and vessel were 0.41 and 0.15 (22% and 14.8%), respectively, that is in line with results from other groups (e.g., 13.8% [11]). The difficulty with this phantom was creating a uniform melanin layer (around 100-300 μm thick) with comparable thickness to the human pigmented layer [28]. However, because of the time-resolved selection of the PA signals from the vessels, the heterogeneity of this layer did not significantly influence the PA data from vessels and moving target's phantom.

5. Conclusions

In this study, we demonstrated a new dynamic blood phantom designed specifically for the PAFC platform to test its real-time detection of circulating objects with positive and negative contrasts. The phantom's optical (absorption and scattering), geometrical (mimic vessel and cell sizes), and dynamic (flow velocity) properties are similar to those of human tissue. Over a few days, the PA signals from the phantom of skin and vessels showed good instability. This phantom can be used to verify new PAFC schematics, calibration, and optimization. In particular, the laser diode demonstrated a promising performance with PAFC for detecting fast moving objects with negative, positive, and combined contrasts in a blood background.

Funding

RF Government (14.Z50.31.0044); NIH (R01CA131164 and R01EB017217); NSF (OIA 1457888 and DBI 1556068).

Acknowledgments

We thank I. Pelivanov (Univ. of Washington) and Q. Zhou (Univ. of Southern California) for providing the customized focused cylindrical and spherical transducers, respectively and thank S. Nikitin, Y. Menyaev, and D. Nedosekin for helping with initial a laser diode and phantom testing.

Disclosures

The authors declare that there are no conflicts of interest.

References

1. V. V. Tuchin, A. Tárnok, and V. P. Zharov, "In vivo flow cytometry: a horizon of opportunities," Cytometry A **79**(10), 737–745 (2011).
2. E. I. Galanzha and V. P. Zharov, "Photoacoustic flow cytometry," Methods **57**(3), 280–296 (2012).

Biomedical Optics EXPRESS

3. E. I. Galanzha and V. P. Zharov, "Circulating tumor cell detection and capture by photoacoustic flow cytometry in vivo and ex vivo," Cancers (Basel) **5**(4), 1691–1738 (2013).
4. C. Cai, K. A. Carey, D. A. Nedosekin, Y. A. Menyaev, M. Sarimollaoglu, E. I. Galanzha, J. S. Stumhofer, and V. P. Zharov, "In vivo photoacoustic flow cytometry for early malaria diagnosis," Cytometry A **89**(6), 531–542 (2016).
5. Y. A. Menyaev, K. A. Carey, D. A. Nedosekin, M. Sarimollaoglu, E. I. Galanzha, J. S. Stumhofer, and V. P. Zharov, "Preclinical photoacoustic models: application for ultrasensitive single cell malaria diagnosis in large vein and artery," Biomed. Opt. Express **7**(9), 3643–3658 (2016).
6. C. Cai, D. A. Nedosekin, Y. A. Menyaev, M. Sarimollaoglu, M. A. Proskurnin, and V. P. Zharov, "Photoacoustic flow cytometry for single sickle cell detection in vitro and in vivo," Anal. Cell Pathol. (Amst.) **2016**, 2642361 (2016).
7. J. Nolan, M. Sarimollaoglu, D. A. Nedosekin, A. Jamshidi-Parsian, E. I. Galanzha, R. A. Kore, R. J. Griffin, and V. P. Zharov, "In vivo flow cytometry of circulating tumor-associated exosomes," Anal. Cell Pathol. (Amst.) **2016**, 1628057 (2016).
8. E. I. Galanzha, M. Sarimollaoglu, D. A. Nedosekin, S. G. Keyrouz, J. L. Mehta, and V. P. Zharov, "In vivo flow cytometry of circulating clots using negative photothermal and photoacoustic contrasts," Cytometry A **79**(10), 814–824 (2011).
9. D. A. Nedosekin, M. Sarimollaoglu, E. I. Galanzha, R. Sawant, V. P. Torchilin, V. V. Verkhusha, J. Ma, M. H. Frank, A. S. Biris, and V. P. Zharov, "Synergy of photoacoustic and fluorescence flow cytometry of circulating cells with negative and positive contrasts," J. Biophotonics **6**(5), 425–434 (2013).
10. D. A. Nedosekin, T. Fahmi, Z. A. Nima, J. Nolan, C. Cai, M. Sarimollaoglu, E. Dervishi, A. Basnakian, A. S. Biris, and V. P. Zharov, "Photoacoustic flow cytometry for nanomaterial research," Photoacoustics **6**, 16–25 (2017).
11. S. E. Bohndiek, S. Bodapati, D. Van De Sompel, S. R. Kothapalli, and S. S. Gambhir, "Development and application of stable phantoms for the evaluation of photoacoustic imaging instruments," PLoS One **8**(9), e75533 (2013).
12. W. C. Vogt, C. Jia, K. A. Wear, B. S. Garra, and T. Joshua Pfefer, "Biologically relevant photoacoustic imaging phantoms with tunable optical and acoustic properties," J. Biomed. Opt. **21**(10), 101405 (2016).
13. M. Fonseca, B. Zeqiri, P. Beard, and B. Cox, "Characterization of a PVCP based tissue-mimicking phantom for Quantitative Photoacoustic Imaging," Proc. SPIE - Int. Soc. Opt. Eng. **9539**, 953911 (2015).
14. M. Fonseca, B. Zeqiri, P. C. Beard, and B. T. Cox, "Characterisation of a phantom for multiwavelength quantitative photoacoustic imaging," Phys. Med. Biol. **61**(13), 4950–4973 (2016).
15. J. Laufer, E. Zhang, and P. Beard, "Evaluation of absorbing chromophores used in tissue phantoms for quantitative photoacoustic spectroscopy and imaging," IEEE J. Sel. Top. Quantum Electron. **16**(3), 600–607 (2010).
16. G. M. Spirou, A. A. Oraevsky, I. A. Vitkin, and W. M. Whelan, "Optical and acoustic properties at 1064 nm of polyvinyl chloride-plastisol for use as a tissue phantom in biomedical optoacoustics," Phys. Med. Biol. **50**(14), N141–N153 (2005).
17. W. Xia, D. Piras, M. Heijblom, W. Steenbergen, T. G. van Leeuwen, and S. Manohar, "Poly(vinyl alcohol) gels as photoacoustic breast phantoms revisited," J. Biomed. Opt. **16**(7), 075002 (2011).
18. C. Avigo, N. Di Lascio, P. Armanetti, C. Kusmic, L. Cavigli, F. Ratto, S. Meucci, C. Masciullo, M. Cecchini, R. Pini, F. Faita, and L. Menichetti, "Organosilicon phantom for photoacoustic imaging," J. Biomed. Opt. **20**(4), 046008 (2015).
19. W. C. Vogt, C. Jia, K. A. Wear, B. S. Garra, and T. Joshua Pfefer, "Biologically relevant photoacoustic imaging phantoms with tunable optical and acoustic properties," J. Biomed. Opt. **21**(10), 101405 (2016).
20. A. V. Bykov, A. P. Popov, A. V. Priezzhev, and R. Myllylä, "Multilayer tissue phantoms with embedded capillary system for OCT and DOCT imaging," in *Proceedings of SPIE 8091, Optical Coherence Tomography and Coherence Techniques V*, 80911R (2011).
21. N. Hungr, J. A. Long, V. Beix, and J. Troccaz, "A realistic deformable prostate phantom for multimodal imaging and needle-insertion procedures," Med. Phys. **39**(4), 2031–2041 (2012).
22. S. E. Bohndiek, S. Bodapati, D. Van De Sompel, S. R. Kothapalli, and S. S. Gambhir, "Development and application of stable phantoms for the evaluation of photoacoustic imaging instruments," PLoS One **8**(9), e75533 (2013).
23. L. C. Cabrelli, P. I. Pelissari, A. M. Deana, A. A. O. Carneiro, and T. Z. Pavan, "Stable phantom materials for ultrasound and optical imaging," Phys. Med. Biol. **62**(2), 432–447 (2017).
24. Y. Sun, H. Jiang, and B. E. O'Neill, "Photoacoustic imaging: An emerging optical modality in diagnostic and theranostic medicine," J. Biosens. Bioelectron. **2**(108), 1000108-1(2011).
25. J. L. Sandell and T. C. Zhu, "A review of in-vivo optical properties of human tissues and its impact on PDT," J. Biophotonics **4**(11-12), 773–787 (2011).
26. Y.A. Menyaev, D.A. Nedosekin, M. Sarimollaoglu, M.A. Juratli, E.I. Galanzha, V.V. Tuchin, and V.P. Zharov, "Optical clearing in photoacoustic flow cytometry," Biomed. Opt. Express **4**(12), 3030–3041 (2013).
27. J. E. Thatcher, K. D. Plant, D. R. King, K. L. Blocka, W. Fan, and J. M. DiMaioa, "Dynamic tissue phantoms and their use in assessment of a non-invasive optical plethysmography imaging device," Proc. SPIE **9107**, 910718 (2014).

Biomedical Optics EXPRESS

28. D. Korugaa, J. Bandi, G. Janji, C. Lalovic, J. Muncanc, and D. Dobrosavljevi Vukojevi, "Epidermal layers characterization by opto-magnetic spectroscopy based on digital image of skin," Acta Phys. Pol. A **121**(3), 606–610 (2012).